Acta Universitatis Sapientiae

Electrical and Mechanical Engineering

Volume 13, 2021

Sapientia Hungarian University of Transylvania
Scientia Publishing House

Contents

Acta Universitatis Sapientiae
Electrical and Mechanical Engineering, 13 (2021) 1–13

DOI: 10.2478/auseme-2021-0001

Process Optimization of PVDF Piezoelectric Nanofiber Production via Electrospinning

Attila Levente GERGELY[1], József KÁNTOR[2]

Sapientia Hungarian University of Transylvania, Cluj-Napoca,
Faculty of Technical and Human Sciences, Târgu Mureș,
Department of Mechanical Engineering,
e-mail: [1]agergely@ms.sapientia.ro, [2]kantorjozsef@ms.sapientia.ro

Manuscript received October 20, 2021; revised November 01, 2021

Abstract: The aim of this work was to investigate the effect of processing parameters of the electrospinning method on the resulting poly (vinylidene fluoride) (PVDF) fiber diameter. A three factorial Box-Behnken experimental design was employed to study the influence of applied voltage, the capillary-to-collector distance and the applied flow rate on the resulting fiber diameter. We successfully prepared bead-free PVDF nanofibers with fiber diameters ranging from 510-1300 nm. The experimental design analysis did not show significant influence of the studied process parameters under the used boundary conditions on the fiber diameter, thus indicating the robustness of the process.

Keywords: PVDF, electrospinning, nanofiber, piezoelectricity, polymer processing.

1. Introduction

There is a constant need to develop better and more efficient processes for sensor applications. In this respect the use of nanofibers offers high potential in several applications due to their unique properties. The deposition of nanofibers provides a fiber mat, a structure that has a high surface-area-to-volume ratio. The surface-to-volume ratio is inversely proportional to the characteristic cross-sectional dimension of the fibers - usually referred to as fiber diameter, as most fibers have near-circular cross-section. Taking advantage of this property, research groups experimented with fiber mats in multiple domains, some noteworthy applications being filters, scaffolds for cell growth, carriers for drug delivery, catalysis, sensors and actuators [1], [2].

Electrospinning is a widely used method to create polymeric fibers, due to the simplicity of its setup for small scale production under laboratory

conditions. The process involves the placement of a polymer solution droplet into an electric field, while the droplet is in contact with the positive electrode of the instrument. When there is adequate positive charge buildup on the surface of the droplet, it starts to deform, creating the Taylor cone. Eventually the electrostatic forces overcome the surface tension and an electrified jet is created [3]. If new solution is fed into the droplet with the appropriate volumetric flow rate, the Taylor cone and the jet can be maintained at a steady state. The electrified jet travelling from the positive electrode to the grounded electrode (collector) gets elongated by the Coulomb forces and in the process it loses mass by solvent evaporation. At some point the thinning jet becomes unstable due to the increasing volumetric charge density, arranging itself into a coil-like shape and starts a whipping motion. This is called the bending instability, and it causes the jet to travel a much longer distance until reaching the collector than a straight line between the positive electrode and the collector [4]. The elongation of the jet proceeds until it either reaches the collector or dries out enough that the viscoelastic forces become stronger than the Coulomb forces.

The size and morphology of the polymeric fibers produced with electrospinning have a great variety, depending on the materials involved and the process parameters. The fiber sizes range from several micrometers to tens of nanometers, but the most common is the several hundreds of nanometers. The fibers are usually deposited in a random manner (non-woven fiber mats), and extra effort is required to orient the fibers in certain ways. The different fiber mat morphologies can provide different uses [5], [6]. It was found that in keratinocyte cell cultures cell proliferation in a PVA fiber mat with fiber size of 70 nm wasn't different from the control (natural extracellular matrix), while 300 nm fibers resulted in a 100% increase in cell proliferation during a 5-day period. Further increasing the fiber size to 1000 nm caused a decrease in cell proliferation rate compared to 300 nm, but it was still 30% higher than the control [5]. Bian *et al.* published results on filters made of nylon fibers which showed that the removal efficacy of particles (size smaller than 2.5 μm) was close to 98% at ~50 nm fiber size, and gradually dropped to 60% as fiber size increased to 250 nm. [6]

Thus, it is desirable to control the morphological aspects (e.g. fiber size, porosity, orientation, packing density, presence of beads) of the created fiber mats, and to determine which process parameter affects these the most.

Focusing on the fiber size, according to theory, the higher the volumetric charge density in a certain jet segment, the stronger the tensile force, thus the more intensive the elongation. Increasing the voltage increases the volumetric charge density in the solution [7], and in the model system of polyethylene oxide (PEO)/water it was proven that electrospinning at higher charge densities yields thinner fibers [8]. The distance between the positive and the grounded

electrode (needle-collector, NC distance) has multiple ways of interacting with the fiber size. At a given voltage the longer NC distance yields lower electric field strength, and thus causes the weakening of the electrostatic forces [7]. However, a longer NC distance also allows more time for the jets to elongate and for the solvent to evaporate. The rate of solvent evaporation is also crucial as it influences the viscoelastic properties of the jet [3], [9]. Other important factors include solution viscosity, ambient temperature and relative humidity, surface tension, relaxation delay [10].

Published experimental data on the correlation of electrospinning parameters and fiber size is somewhat controversial. For example some studies showed that increasing the applied voltage made the produced fibers thinner [11]–[13], but there are also studies that showed the opposite effect [14]. This indicates that, as of now, there is no generally applicable model for all polymer/solvent systems, and each system has to be studied individually in order to find the optimal electrospinning conditions.

Polyvinylidene fluoride (PVDF) is a semi-crystalline polymer that could exhibit piezoelectric properties [15]. There are five known crystal phases (α, β, γ, δ, ε), [16] and the β-phase and to a lesser extent the γ- and δ-phases contribute to the piezoelectic behavior. The β-phase is the parallel packing of the all-anti configuration of PVDF molecules (also referred to as all-trans in the relevant literature), which is polar in nature and capable of inducing the highest dipole moments out of all the crystal phases [17]. Due to its thermodynamic stability, the α-phase is usually overrepresented in the produced PVDF films. The transition from α- to β-phase was initially achieved with energy-intensive procedures requiring pressures up to 5000 atm and 285°C [17]. More recently electrical poling has been used, that involves the stretching of the sheet at elevated temperature and placing it in an electric field of 10^7 V/m order of magnitude [18].

During electrospinning PVDF undergoes a process similar to poling. The stretching of the fibers and the strong electric field facilitates the formation of β-phase [19]. Experimental data showed that in electrospun fiber mats the β-phase content can reach 85-90% [19], [20]. The electrospinning of PVDF has been successfully used on multiple occasions to create fiber mats that exhibited piezoelectric properties and subsequently devices that incorporated these fiber mats. [21]–[23]

The aim of this work was to determine the significance of the electrospinning process parameters on the resulting PVDF fiber diameter. Thus, a three factorial Box-Behnken experimental design was used, in which the applied voltage, the needle-to-collector distance and the flow rate were selected as factors. In addition, the presence of β and γ crystalline phases in the PVDF

nanofibers were confirmed by FTIR. A simple setup was used to determine the sensitivity of the produced piezoelectric PVDF fiber mats.

2. Experimental

2.1. Materials

Polyvinylidene fluoride (PVDF) (MFI 8g/10min, at 2.16 kg and 230 °C, ASTM D1238, Songhan Plastic Technology), acetone (ACS grade, Sigma Aldrich) and dimethyl formamide (DMF, ACS grade, Sigma Aldrich) were used as received.

2.2. Polymer Solution

20 wt% PVDF in 1:1 acetone:DMF (v:v) solution concentration was selected based on preliminary experiment. To dissolve the PVDF in the solvent mixture ultrasonication was employed at 70 °C for 3 hours, resulting in a clear viscous polymer solution.

2.3. Electrospinning

Electrospinning was carried out on a custom-built apparatus [24]. The PVDF solution was placed into a syringe, and the constant flow rate was ensured by a syringe pump (Fisher Scientific). The syringe was connected to a G21 needle via PTFE tubing. The collector was covered with Al foil and placed at the desired distance from the needle. The positive potential of the DC high voltage supply (Gamma Scientific) was connected to the needle and the collector was grounded. The electrospinning process was carried out at ~21 °C and ~30 % relative humidity.

2.4. Scanning Electron Microscopy (SEM)

The fiber mat morphology was examined with a JEOL JSM-5200 scanning electron microscope at 10 kV potential on neat, not sputter coated, samples. To calculate the fiber diameter at least 50 measurements per sample were averaged. ImageJ software was used to measure the fiber diameters.

2.5. Fourier-Transform Infrared Spectroscopy (FTIR)

Infrared spectra of the PVDF nanofibers were collected using a Frontier, PerkinElmer instrument in ATR (attenuated total reflection) mode between 600 - 1500 cm^{-1} wave number, with a resolution of 1 cm^{-1}.

2.6. Experimental Design

The Box-Behnken experimental design (BBD) was generated with the MiniTab software. The applied voltage (V), the needle-to-collector distance (ND) and the flow rate (F) of the polymer solution were selected as factors. *Table 1* shows the boundary limits determined by scouting experiments to produce a stable electrospinning process. The reason we chose the BBD is that it is almost as powerful as a full factorial design but being a fractional factorial design, it requires significantly fewer experiments. With 3 factors it is 27 runs against 15 in favor of the BBD, and thus more efficient in terms of time commitment and resources. A trade-off is that the BBD is less robust, as each data point is critical to the model.

Table 1. Box-Behnken experimental design limits

Electrospinning parameter	**Low (-1)**	**Mid (0)**	**High (+1)**
Flow rate [mL/h]	0.4	0.7	1
Voltage [kV]	14	17	20
Needle-to-collector distance [cm]	10	15	20

3. Results and Discussion

3.1. Fiber morphology

The fiber morphology and fiber diameter were determined by SEM investigation. The SEM images of some samples are shown in *Fig. 1*. The images as well as the tabulated data in *Table 2* illustrate that out of the 15 experimental condition sets, only three produced PVDF fiber mats without beads. As it is illustrated, beads-on-fiber formation is prominent in the samples. It has been reported that in model systems with PEO low viscosity and high surface tension of the solution, and low charge density (which correlates with low applied voltage) favor the formation of beaded fibers [8]. Since there weren't any viscosity or surface tension measurements performed on the PVDF solutions, it can only be proposed that the same applies here as well. Based on our observations the viscosity of the used PVDF solutions was high enough for continuous fiber formation (as the SEM images show). The produced fibers were smooth surfaced and have circular cross section.

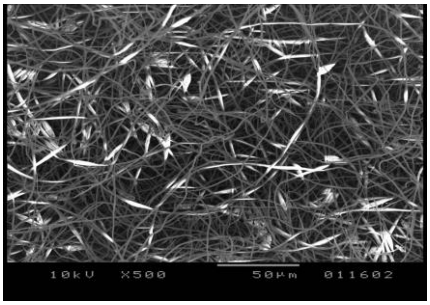

PVDF2

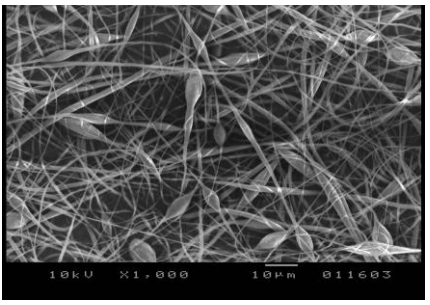

PVDF3

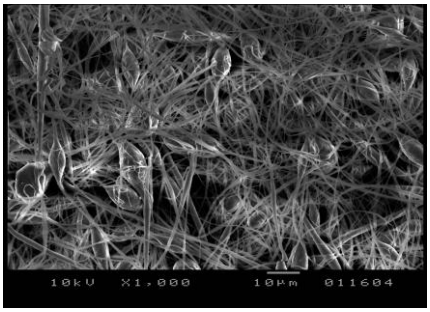

PVDF4

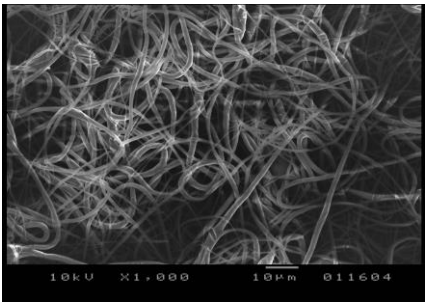

PVDF5

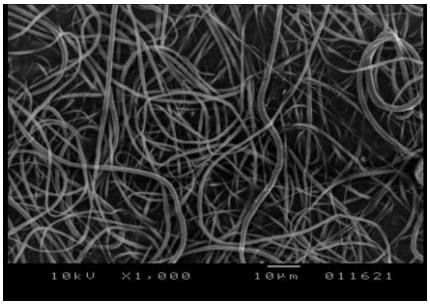

PVDF9

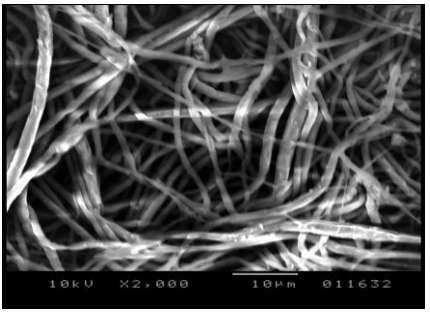

PVDF11

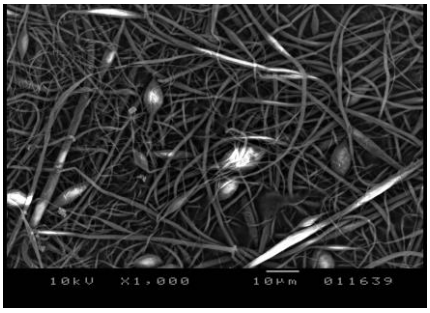

PVDF13

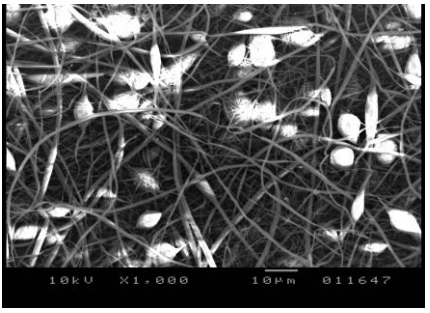

PVDF15

Figure 1: Representative SEM images of the tested samples

Table 2 presents the generated parameter sets for the BBD. Samples named PVDF5, PVDF9 and PVDF11 are the ones that did not contain beads. It can also be noted that the fiber diameters range from 510 nm to 1300 nm

Table: Fiber diameter and standard deviations.

Name	Needle-collector distance [cm]	Volumetric flow rate [mL/h]	Voltage [kV]	Fiber size, d [µm]	Stdev. d [µm]	Bead
PVDF1	15	0.7	17	0.70	0.36	Yes
PVDF2	15	0.4	14	1.30	0.55	Yes
PVDF3	20	0.7	14	0.93	0.52	Yes
PVDF4	15	1	14	0.73	0.45	Yes
PVDF5	10	1	17	1.09	0.44	No
PVDF6	15	0.7	17	0.92	0.38	Yes
PVDF7	15	0.7	17	0.80	0.36	Yes
PVDF8	10	0.7	14	0.51	0.25	Yes
PVDF9	10	0.7	20	0.92	0.23	No
PVDF10	15	1	20	1.07	0.36	Yes
PVDF11	20	0.7	20	1.24	0.36	No
PVDF12	20	0.4	17	1.11	0.44	Yes
PVDF13	15	0.4	20	1.06	0.46	Yes
PVDF14	10	0.4	17	0.92	0.25	Yes
PVDF15	20	1	17	0.76	0.40	Yes

3.2. Experimental design analysis

To investigate the effect of the electrospinning parameters on the fiber size and spread a 3-factor BBD was created. *Tables 3* and *4*, show the respective ANOVA tables.

Table 3: ANOVA table for fiber diameter of the studied fiber mats

Source	DF	Adj. SS	Adj MS	F-value	p-value
Linear	**3**	**0.13734**	**0.04578**	**1.22**	**0.393**
dist	1*	0.01051	0.01051	0.28	0.619
flow	1*	0.0931	0.0931	2.49	0.176
volt	1*	0.030637	0.030637	0.82	0.407
Square	3	0.103227	0.034409	0.92	0.495
Interaction	3	0.154200	0.051400	1.37	0.352
Residual Error	5	0.187167	0.037433		
Total	14				
R-Sq = 70.85% R-Sq(adj) = 18.38% *-accounted for in the DF of Linear source					

The data in *Table 3* shows, that for the fiber diameter, none of the p-values were lower than 0.05 (the lowest being 0.176) and as such the effects of the selected electrospinning parameters indicated no statistical significance in the 95% confidence interval. A study done by Motamedi *et al.* showed that the diameter of PVDF nanofibers electrospun from dimethylacetamide/acetone mixture increased with increasing voltage (300 nm at 10 kV to 855 nm at 20 kV) and decreased with increasing distance (644 nm at 14 cm to 264 nm at 20 cm) [25]. On the other hand, according to the results published by Ribeiro *et al.* average fiber sizes spun from DMF solution decreased from 495 to 403 nm when they increased the voltage from 15 to 30 kV [20]. Neither publication provides statistical data, so the statistical significance of the results is unknown. While not observed for all material/solvent systems (as the first example shows, [25]), it is expected in general that a higher voltage through an increased volumetric charge density and larger tensile forces would yield thinner fibers [8]. As the opposite effect, larger distances would yield thicker fibers because of the weaker electric field and lower charge density [7]. It is theorized that in the case when fibers get thicker with increasing voltage/ higher charge density it is because more solution is drawn from the source and the increased volumetric flow rate results in a thicker jet [14]. In the previously mentioned study with PVDF there wasn't a clear correlation between volumetric flow rate and deposited fiber size [25].

Table 4: ANOVA table for fiber diameter standard deviation of the studied fiber mats

Source	**DF**	**Adj. SS**	**Adj MS**	**F-value**	**p-value**
Linear	**3**	0.031937	0.010646	**2.28**	**0.197**
dist	1*	0.025345	0.025345	5.42	0.067
flow	1*	0.001186	0.001186	0.25	0.636
volt	1*	0.001035	0.001035	0.22	0.658
Squared	3	0.028652	0.009551	2.04	0.227
Interaction	3	0.018125	0.006042	1.29	0.373
Residual Error	5	0.023392	0.004678		
Total	14				
R-Sq = 81.21% R-Sq(adj) = 47.39% *-accounted for in the DF of Linear source					

For the standard deviation of the fiber size, *Table 4*, the distance had a p-value 0.067, which is close to 0.05. While technically not significant by to the chosen convention of the <5% probability for the null hypothesis, it still might be an indication that the widening of the fiber size distribution with the increasing needle-collector distance is not entirely due to randomness. This trend can be observed in the data of Motamedi *et al.* as well, even though the deviation in their samples was roughly an order of magnitude lower [25]. A possible explanation is found in the relationship between solvent evaporation

and the needle-collector distance. It is known that the elongation of the fibers is limited by the drying process [6]. In each electrospinning setup, especially in the more unstable systems there is a variation in the initial jet diameter (i.e. close to the Taylor cone). The initially thin jet segments dry out quickly, and after that point no additional distance will affect the fiber size. On the other hand, for the initially thick jet segments there is more time for the solvent to evaporate if the distance is longer, and thus the result will be a narrower size distribution.

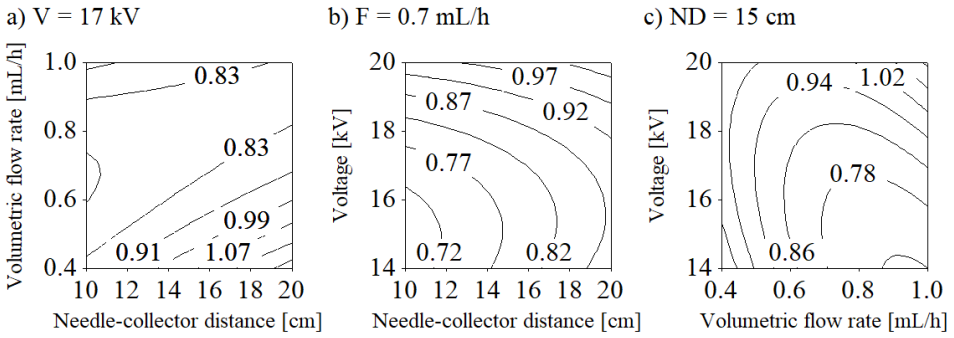

Figure 2: Contour plots of the mean fiber diameter, d [μm], versus a) F-ND, b) V-ND, and c) V-F when the respective third parameter was held at its middle value

While the statistical analysis indicated no significance for the effect of the electrospinning parameters on fiber diameter, some conclusions regarding the process can be drawn from the observations. The contour plots seen in *Fig. 2* show that in the studied region increasing the voltage caused an increase in average fiber size from 600 to 900 nm at F = 0.7 mL/h and ND = 10 cm (*Fig. 2b*), and from 700 to 1000 nm at F = 1 mL/h and ND = 15 cm (*Fig. 2c*). The increase in distance also resulted in thicker fibers in general (*Fig. 2a-b*). Increasing the flow rate caused the average fiber size to decrease. At V = 14 kV and ND = 15 cm it went down from 1100 nm to 700 nm (*Fig. 2c*) and at V = 17 kV, ND = 20 cm from 1200 nm to 800 nm (*Fig. 2a*), however in both cases it seems to have reached a local minimum, after which the fiber size would have started increasing again if the flow rates were to become higher. The low distance favored more uniform fibers, and at higher voltages the bead formation became less prevalent. The most stable condition was at 10 cm distance, 20 kV, and 0.7 mL/h (sample PVDF9), with the fiber mat having submicron fiber size, one of the narrowest fiber size distributions, and no beads.

3.3. Piezoelectric properties

The presence of β and γ crystalline phases, thus the piezoelectric properties of the samples were confirmed by FTIR spectroscopy. A representative FTIR spectrum can be seen in *Fig. 3*. Based on the work of Cai *et al.* the β and γ crystalline phase content relative to the α phase was calculated for each sample, using eq. (1):

$$F_{EA} = \frac{I_{EA}}{\left(\frac{K_{840}}{K_{763}}\right) I_{763} + I_{EA}} \tag{1}$$

where F_{EA} represents the β and γ crystalline phase percentage, I_{EA} and I_{763} represents the absorbance values at 840 and 763 cm^{-1} respectively, whereas K_{840} = 7.7*10^4 and K_{763} = 6.1*10^4 cm^2/mol are the absorbance coefficients at the particular wave number [26]. The FTIR spectra was normalized at ware number 1072 cm^{-1}, since the absorbance of this band is influenced only by the thickness of the sample and not the crystalline structure [27].

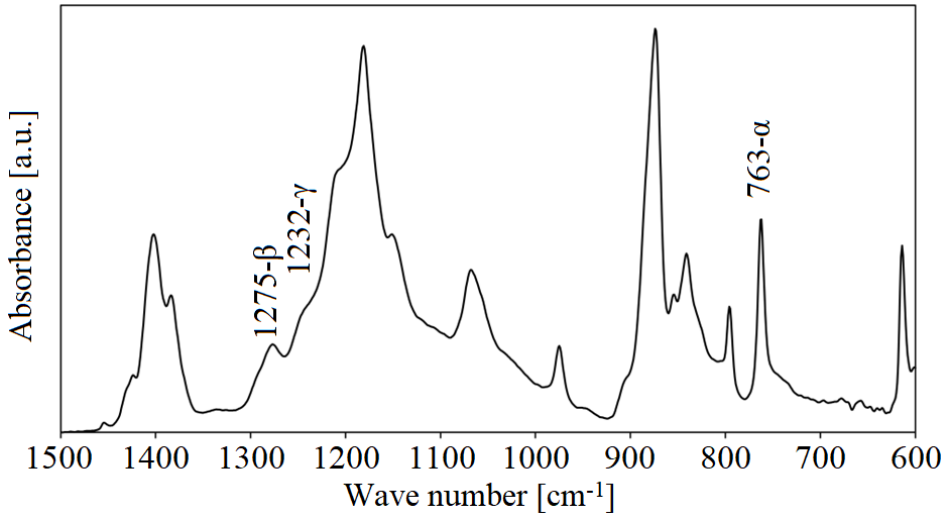

Figure 3: Representative FTIR spectrum

The calculated β and γ crystalline phases for all the samples were within 36-42% with respect to the α phase. To test the piezoelectric properties of the samples a test cell was built in which the samples were placed between two masked copper plates and were subjected to compression forces, while the generated voltage was measured. The samples generated potential difference in response to the loading, however the highest sensitivity (generated

voltage/applied force) of 0.027 mV/N was obtained for sample PVDF11 with 11 μm thickness. The control, 100 μm thick PVDF film produced 0.063 mV/N sensitivity. Thus, the sensitivity of the prepared PVDF nanofiber samples was in the same order of magnitude as the sensitivity of the commercially available PVDF film.

4. Conclusion

In summary, we successfully prepared bead-free smooth surfaced PVDF fiber mats with piezoelectric properties. The 3-factorial Box-Behnken experimental design did not show significant influence of the studied electrospinning parameters on the resulting fiber diameter, thus indicating the robustness of the process. FTIR study confirmed the presence of the electroactive β and γ crystalline phases in all samples in the range of 36-42 % with respect to the α phase. The sensitivity of the electrospun piezoelectric PVDF nanofiber samples was comparable to the control, a commercially available PVDF film.

Acknowledgements

Attila Levente Gergely wishes to thank the Transylvanian Museum Society for the financial support, contract nr. 220.10.1/2020. The authors wish to thank the technical support for Peter Johannes and dr. Marcus Stommel for the FTIR study and the sensor sensitivity measurements.

References

[1] Xue, J., Wu, T., Dai, Y., and Xia, Y., "Electrospinning and electrospun nanofibers: Methods, materials, and applications", *Chem. Rev.*, vol. 119, no. 8, pp. 5298–5415, 2019.

[2] Sipos, E. *et al.*, "Preparation and characterization of fenofibrateloaded PVP electrospun microfibrous sheets", *Pharmaceutics*, vol. 12, no. 7, 2020.

[3] Yarin, A. L., Koombhongse, S., and Reneker, D. H., "Taylor cone and jetting from liquid droplets in electrospinning of nanofibers", *J. Appl. Phys.*, vol. 90, no. 9, pp. 4836–4846, 2001.

[4] Yarin, A. L., Koombhongse, S., and Reneker, D. H., "Bending instability in electrospinning of nanofibers", *J. Appl. Phys.*, vol. 89, no. 5, pp. 3018–3026, 2001.

[5] Pelipenko, J., Kocbek, P., and Kristl, J., "Nanofiber diameter as a critical parameter affecting skin cell response", *Eur. J. Pharm. Sci.*, vol. 66, pp. 29–35, 2015.

[6] Bian, Y., Wang, S., Zhang, L., and Chen, C., "Influence of fiber diameter, filter thickness, and packing density on PM2. 5 removal efficiency of electrospun nanofiber air filters for indoor applications", *Build. Environ.*, vol. 170, p. 106628, 2020.

[7] Theron, S. A., Zussman, E., and Yarin, A. L., "Experimental investigation of the governing parameters in the electrospinning of polymer solutions", *Polymer (Guildf).*, vol. 45, no. 6, pp. 2017–2030, 2004.
[8] Fong, H., Chun, I., and Reneker, D. H., "Beaded nanofibers formed during electrospinning", *Polymer (Guildf).*, vol. 40, no. 16, pp. 4585–4592, 1999.
[9] Tripatanasuwan, S., Zhong, Z., and Reneker, D. H., "Effect of evaporation and solidification of the charged jet in electrospinning of poly (ethylene oxide) aqueous solution", *Polymer (Guildf).*, vol. 48, no. 19, pp. 5742–5746, 2007.
[10] Thompson, C. J., Chase, G. G., Yarin, A. L., and Reneker, D. H., "Effects of parameters on nanofiber diameter determined from electrospinning model", *Polymer (Guildf).*, vol. 48, no. 23, pp. 6913–6922, 2007.
[11] Amiraliyan, N., Nouri, M., and Kish, M. H., "Effects of some electrospinning parameters on morphology of natural silk-based nanofibers", *J. Appl. Polym. Sci.*, vol. 113, no. 1, pp. 226–234, 2009.
[12] Beachley, V., and Wen, X., "Effect of electrospinning parameters on the nanofiber diameter and length", *Mater. Sci. Eng. C*, vol. 29, no. 3, pp. 663–668, 2009.
[13] Nasouri, K., Bahrambeygi, H., Rabbi, A., Shoushtari, A. M., and Kaflou, A., "Modeling and optimization of electrospun PAN nanofiber diameter using response surface methodology and artificial neural networks", *J. Appl. Polym. Sci.*, vol. 126, no. 1, pp. 127–135, 2012.
[14] Jia, Z., Li, Q., Liu, J., Yang, Y., Wang, L., and Guan, Z., "Preparation and properties of poly (vinyl alcohol) nanofibers by electrospinning", *J. Polym. Eng.*, vol. 28, no. 1–2, pp. 87–100, 2008.
[15] Kawai, H., "The piezoelectricity of poly (vinylidene fluoride)", *Jpn. J. Appl. Phys.*, vol. 8, no. 7, p. 975, 1969.
[16] Lovinger, A. J., "Annealing of poly (vinylidene fluoride) and formation of a fifth phase", *Macromolecules*, vol. 15, no. 1, pp. 40–44, 1982.
[17] Hasegawa, R., Kobayashi, M., and Tadokoro, H., "Molecular conformation and packing of poly (vinylidene fluoride). Stability of three crystalline forms and the effect of high pressure", *Polym. J.*, vol. 3, no. 5, pp. 591–599, 1972.
[18] Ramos, M. M. D., Correia, H. M. G., and Lanceros-Mendez, S., "Atomistic modelling of processes involved in poling of PVDF", *Comput. Mater. Sci.*, vol. 33, no. 1–3, pp. 230–236, 2005.
[19] Gee, S., Johnson, B., and Smith, A. L., "Optimizing electrospinning parameters for piezoelectric PVDF nanofiber membranes", *J. Memb. Sci.*, vol. 563, pp. 804–812, 2018.
[20] Ribeiro, C., Sencadas, V., Ribelles, J. L. G., and Lanceros-Méndez, S., "Influence of processing conditions on polymorphism and nanofiber morphology of electroactive poly (vinylidene fluoride) electrospun membranes", *Soft Mater.*, vol. 8, no. 3, pp. 274–287, 2010.
[21] Lang, C., Fang, J., Shao, H., Ding, X., and Lin, T., "High-sensitivity acoustic sensors from nanofibre webs", *Nat. Commun.*, vol. 7, no. 1, pp. 1–7, 2016.
[22] Wang, Y. R., Zheng, J. M., Ren, G. Y., Zhang, P. H., and Xu, C., "A flexible piezoelectric force sensor based on PVDF fabrics", *Smart Mater. Struct.*, vol. 20, no. 4, p. 45009, 2011.
[23] Fang, J., Wang, X., and Lin, T., "Electrical power generator from randomly oriented electrospun poly (vinylidene fluoride) nanofibre membranes", *J. Mater. Chem.*, vol. 21, no. 30, pp. 11088–11091, 2011.
[24] Gergely, A., Kántor, J., Bitay, E., and Biró, D., "Electrospinning of Polymer Fibres Using Recycled PET", *Acta Mater. Transylvanica*, vol. 2, no. 1, pp. 19–26, 2019.
[25] Motamedi, A. S., Mirzadeh, H., Hajiesmaeilbaigi, F., Bagheri-Khoulenjani, S., and Shokrgozar, M., "Effect of electrospinning parameters on morphological properties of PVDF nanofibrous scaffolds", *Prog. Biomater.*, vol. 6, no. 3, pp. 113–123, 2017.

[26] Cai, X., Lei, T., Sun, D., and Lin, L., "A critical analysis of the $α$, $β$ and $γ$ phases in poly (vinylidene fluoride) using FTIR", *RSC Adv.*, vol. 7, no. 25, pp. 15382–15389, 2017.
[27] Benz, M. and Euler, W. B., "Determination of the crystalline phases of poly (vinylidene fluoride) under different preparation conditions using differential scanning calorimetry and infrared spectroscopy", *J. Appl. Polym. Sci.*, vol. 89, no. 4, pp. 1093–1100, 2003.

Acta Universitatis Sapientiae
Electrical and Mechanical Engineering, 13 (2021) 14–24

DOI: 10.2478/auseme-2021-0002

Investigation of the Thermodynamic Characteristics of the Ester Oil and R152a, R125, R134a and R123 Refrigerant Mixtures

Robert Santa

University of Dunaújváros,
Department of Mechanical Engineering,
e-mail: santar@uniduna.hu

Manuscript received October 07, 2021; revised November 08, 2021.

Abstract: The presence of the lubricant POE 68 in the refrigeration system changes the thermophysical properties of the refrigerant, which significantly affects the heat transfer and the hydraulic processes. The purpose of this research is to investigate the thermodynamic properties of the R152a, R125, R134a and R123 refrigerant and POE 68 lubricant mixtures at different temperatures from 233,15 to 313,15 K. There have been investigated the values of the densities and kinematic viscosities of the mixtures at different concentrations (100%, 90%, 80%). Finally, it was found that, the density and kinematic viscosity of the R123/POE 68 mixture were most affected by the change of the concentration.

Keywords: Heat pump, refrigerant, oil, mixture, density, viscosity

1. Introduction

The modelling of the heat pumps is based on decades of experience as both of stationary [1], [2] and the non-stationary [3], [4] mathematical models. The mathematical models are fraught with a numerous omissions and uncertainties.

The accuracy of the heat pumps models is greatly affected by the accuracy of the pressure drop correlations which are used to determine the pressure drop of the refrigerant flowing in the tubes and the heat transfer correlations [5], [6] which are used to determine the heat transfer coefficients. In the literature, there are a large number of correlations of heat transfer and pressure drop, whose accuracy, validity is uncertain. Last, but not least, a considerable number of them ignore the effect of the oil in the refrigerant, although refrigerant oil is an essential requirement for the operation of the cycle. This study investigated the changes of the density and kinematic viscosity values of the refrigerant R152a,

R125, R134a, R123 and the POE68 polyester oil mixtures as a function of the temperatures. The analysis was performed at high refrigerant concentrations in the mixture. The concentrations were 100%, 90% and 80 %, where 100 % represents the pure refrigerant.

2. Mathematical model

Due to the complexity of the Navier-Stokes differential equations [7] used to describe the flowing refrigerant, it is extremely difficult to obtain an analytical solution. The form of the differential equation used here is:

$$\frac{\mathrm{d}u}{\mathrm{d}t} + u \cdot \nabla u = -\nabla p + \rho \cdot g + \mu \cdot \nabla^2 u \tag{1}$$

where the significance of the terms is the following:

- ∇p pressure gradient (fluid flows in the direction of largest change in pressure);
- $\rho \cdot g$ body force term (external forces, that act on the fluid);
- $\mu \cdot \nabla^2 u$ diffusion term (for a Newtonian fluid, viscosity operates as a diffusion of momentum).

However, in the equations, the resulting characteristic members can be related to each other as ratios, resulting ratios will be dimensionless expressions. The numerical values of the dimensionless expressions – similarity criteria – thus obtained are independent of the unit system used. In the formulation of hydrodynamic similarity criteria, the force of inertia is chosen as the reference basis.

The characteristic terms of the equation [1] can be primed, related to each other, using ratios. It is useful to turn the equation [1] into a dimensionless form. In order to formulate the hydrodynamic similarity criteria, the force of inertia is used as a reference value.

If all members are divided by this value, the result is the dimensionless criteria. The dimensional analysis method is also used to determine the amount of heat transferred during convective heat flow and the heat transfer coefficient.

In general, the heat transfer coefficient of the refrigerant can be determined as a function of the Reynolds number (Re), Prandtl number (Pr) and Grashof number (Gr):

$$\alpha = \frac{\lambda}{d}, f(\mathrm{Re}, \mathrm{Pr}, \mathrm{Gr}) \tag{2}$$

From the above equations it is clear that, in addition to the flow parameters, the characteristics of the refrigerant, i.e. the density and viscosity of the

refrigerant also play a decisive role. In order to analyze the heat pump cycle, it is necessary to determine the thermodynamic parameters of the function lubricant POE68 in order to be able to define thermal and hydraulic processes.

The mathematical equations (3 - 10) are used to compute the kinematic viscosity and the density of the mixtures of 80%, 90% concentration solutions and of the pure 100% refrigerant. The equations are suitable for high refrigerant concentrations and temperatures between -40 °C and 40 °C.

Algebraic equations are used for determining the density of the R134a/POE 68 polyester (pentaerythritol) Ester Mixed Acid and the R123/POE 68 pentaerythritol Ester Mixed Acid [8]:

$$\rho = \left(a_1 + a_2 \cdot T_r + a_3 \cdot T_r^2\right) + \omega \cdot \left(a_4 + a_2 \cdot T_r + a_6 \cdot T_r^2\right) + \omega^2 \cdot \left(a_7 + a_8 \cdot T_r + a_9 \cdot T_r^2\right) \tag{3}$$

where,

$$T_r = 1 - \frac{T}{T_C}$$

Kinematic viscosity is given by

$$\log \vartheta = \left(a_1 + \frac{a_2}{T} + \frac{a_3}{T^2}\right) + \omega \cdot \left(a_4 + \frac{a_5}{T} + \frac{a_6}{T^2}\right) + \omega^2 \cdot \left(a_7 + \frac{a_8}{T} + \frac{a_9}{T^2}\right) \tag{4}$$

and ω is the refrigerant mass fraction.

The following algebraic equations are used for the determination of density and kinematic viscosity of the R125/POE 68 and the R152a/POE 68 pentaerythritol Ester Mixed Acid [8]:

$$\rho_{100} = a_1 + a_2 \cdot T + a_3 \cdot T^2 \tag{5}$$

$$\rho_{90} = a_4 + a_5 \cdot T + a_6 \cdot T^2 \tag{6}$$

$$\rho_{80} = a_7 + a_8 \cdot T + a_9 \cdot T^2 \tag{7}$$

$$\log \vartheta_{100} = a_1 + \frac{a_2}{T} + \frac{a_3}{T^2} \tag{8}$$

$$\log \vartheta_{90} = a_4 + \frac{a_5}{T} + \frac{a_6}{T^2} \tag{9}$$

$$\log \vartheta_{80} = a_7 + \frac{a_8}{T} + \frac{a_9}{T^2} \tag{10}$$

The coefficients are found in [8] and the subscript 100, 90, 80 refer to the mass fraction of the refrigerant.

3. Results and discussion

The figures below summarize the density and kinematic viscosity of the refrigerants R152a, R125, R134a and R123 and of the ester oil lubricant POE 68 as a function of the temperature.

Fig. 1 and *Fig. 2* show the density and kinematic viscosity of a mixture of R152a refrigerant and POE68 oil. In the first figure it can be observed that below the limit of 273.13 K, influence of the concentration on the density, between 80% and 100% is practically insignificant. However, it can also be seen that as the temperature increases, the value of the density of the mixture also decreases considerably.

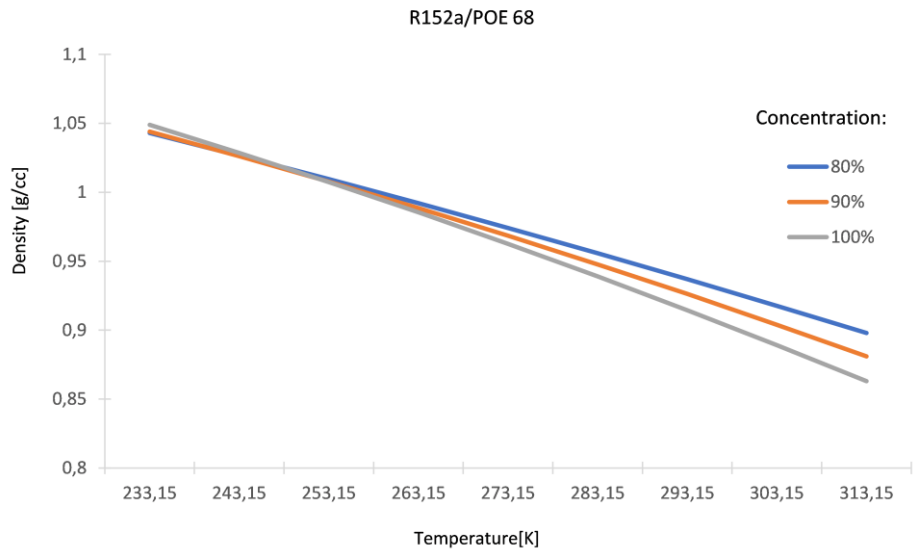

Figure 1: Density of the R152a/POE 68 as a function of the temperature

It can be noticed that at low temperatures 233.15 K and 80% concentration, the kinematic viscosity of the mixture increases significantly, while at higher temperatures 313.5 K, the difference in viscosity values presents less importance at different concentrations.

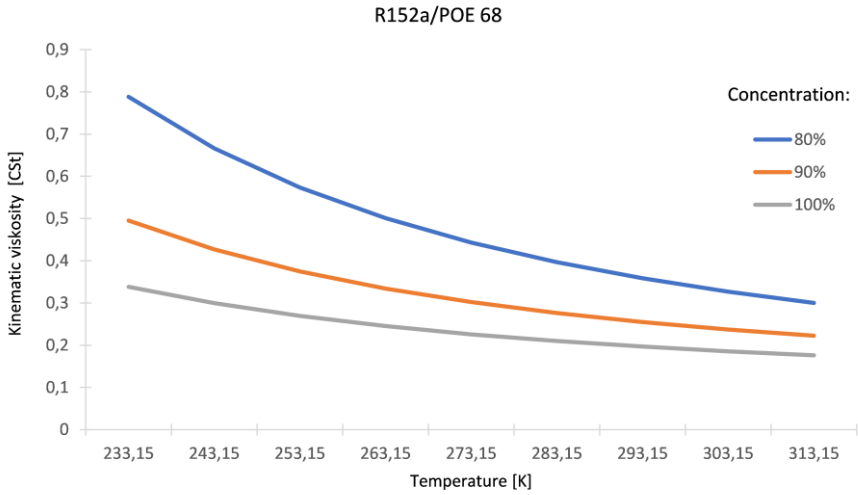

Figure 2: Kinematic viscosity of the R152a/POE 68 as a function of the temperature

The density and the kinematic viscosity of the mixture of R125 and POE68 can be seen in Figures 3 and 4.

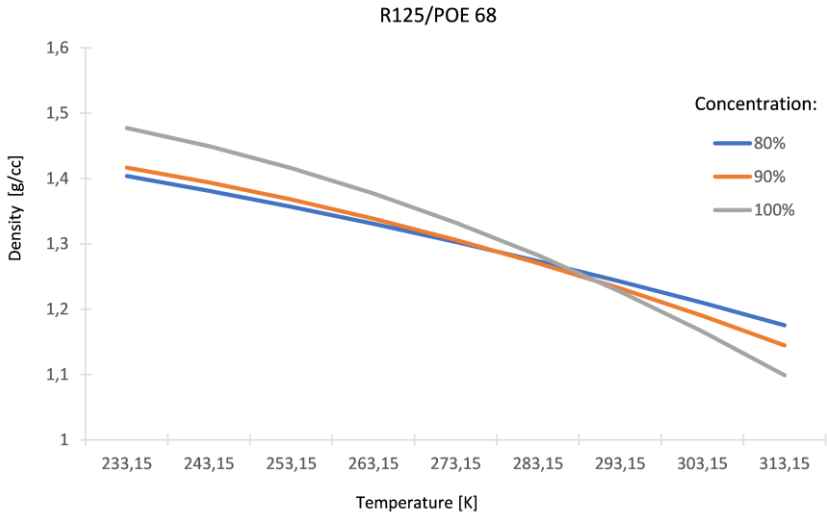

Figure 3: Density of the R125/POE 68 as a function of the temperature

The figure shows that at 283.13 K the density of the mixture is nearly constant for all three concentrations at 80%, 90% and 100%. It can also be seen that as the temperature decreases, and at 100% concentration - pure refrigerant, the value of the refrigerant density is higher than at 80% and 90% concentration, while at a higher temperature of 313.15K the reverse of the phenomenon is observed.

Considering the kinematic viscosity, it is demonstrated that the viscosity value for a pure 100% refrigerant is nearly the same over the temperature range investigated, while for the 80% mixture the viscosity value increases significantly for low temperatures of 233.15 K.

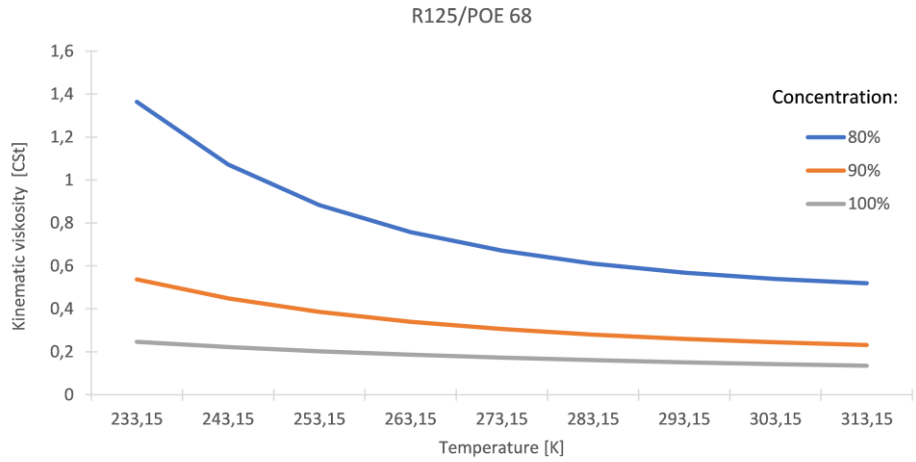

Figure 4: Kinematic viscosity of the R125/POE 68 as a function of the temperature

The density and kinematic viscosity of the mixture of R134a and POE 68 are shown in *Fig. 5* and *Fig. 6*. It can be seen that as the temperature decreases, the density value increases steadily for 80% and 90% concentration, but the highest density values are observed for the pure, i.e., 100% refrigerant.

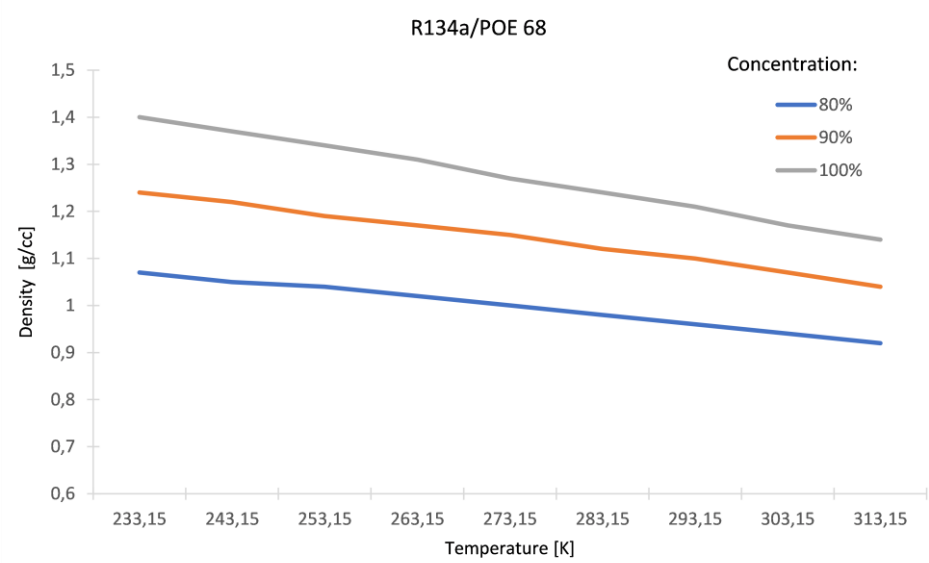

Figure 5: Density of the R134a/POE 68 as a function of the temperature

Fig. 6 shows that at a low temperature of 233.15 K, the kinematic viscosity of a mixture with a concentration of 80% is five times greater than those of the pure refrigerant, whereas at higher temperatures 313.15 K it decreases to nearly the double.

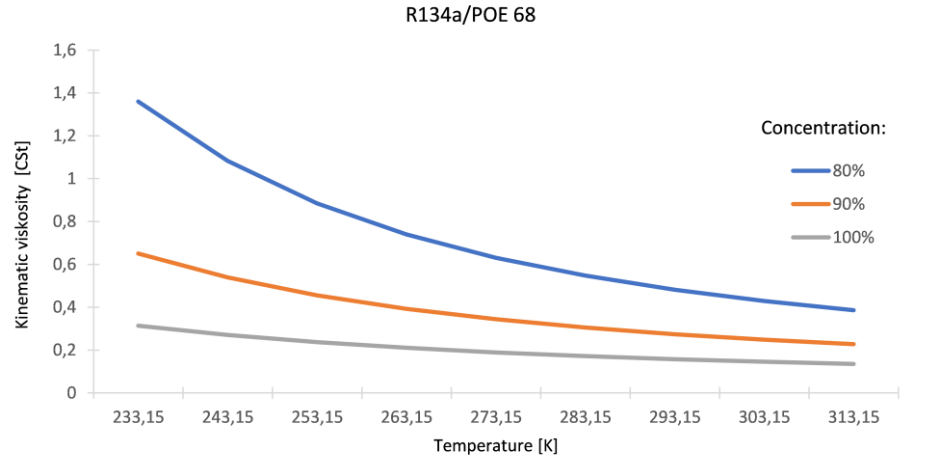

Figure 6: Kinematic viscosity of the R134a/POE 68 as a function of the temperature

The density and kinematic viscosity of the refrigerant R123 and the lubricant POE 68 are summarized in *Fig. 7* and *Fig. 8*. It can be deduced that as the temperature decreases, the density, and the kinematic viscosity values of all three mixtures increase and show the same trend as R134a/POE 68, but presenting larger numerical values, for both thermodynamic parameters.

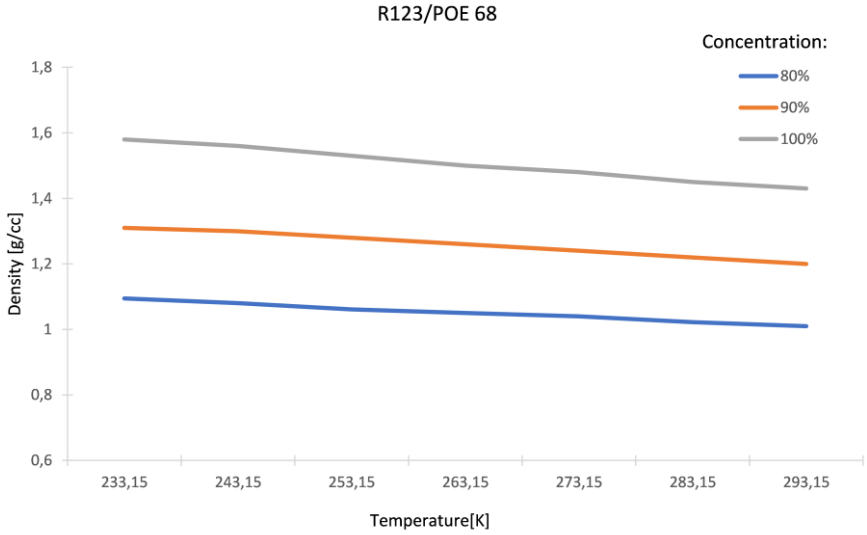

Figure 7: Density of the R123/POE 68 as a function of the temperature

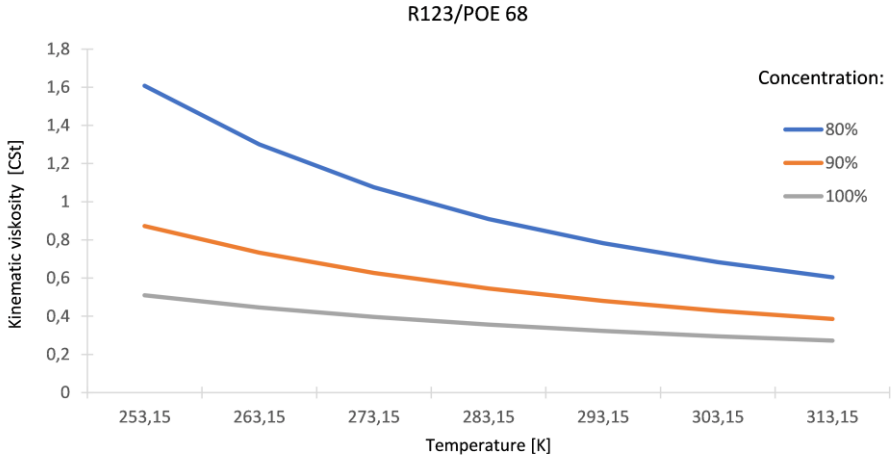

Figure 8: Kinematic viscosity of the R123/POE 68 as a function of the temperature

The following figures show the effect of oil on the change of the heat transfer coefficient by way of a numeric simulation example. In the convective condensation heat transfer correlations [9], [10] the 80% and 90% mixture concentrations were taken into account.

The range of simulation conditions:

- Refrigerant: R134a;
- Vapor quality: 0.1 – 0.9 [-];
- Mass flux: 125, 250 [kg/m^{2}s];
- Concentration: 80% 90%, 100%.

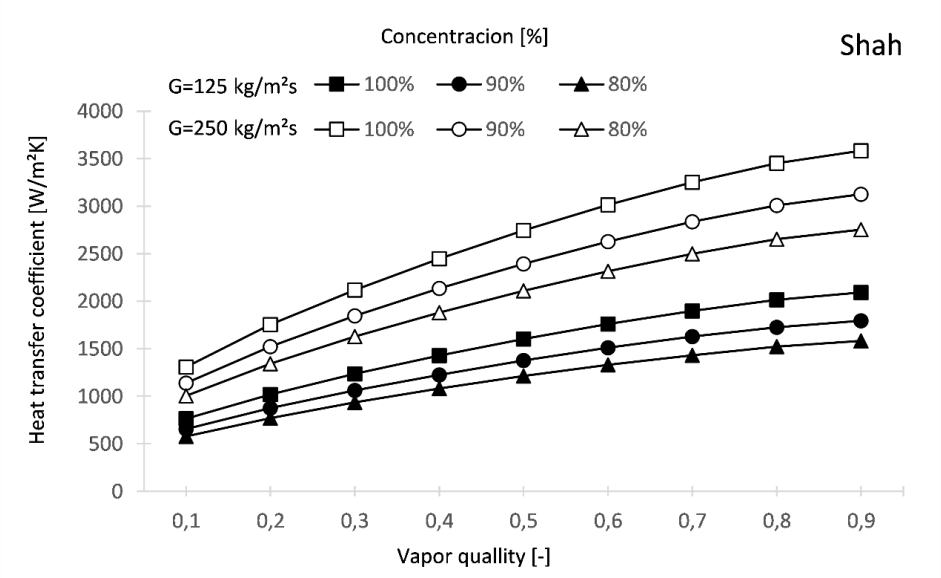

Figure 9: Heat transfer coefficient based on the Shah correlation [9]

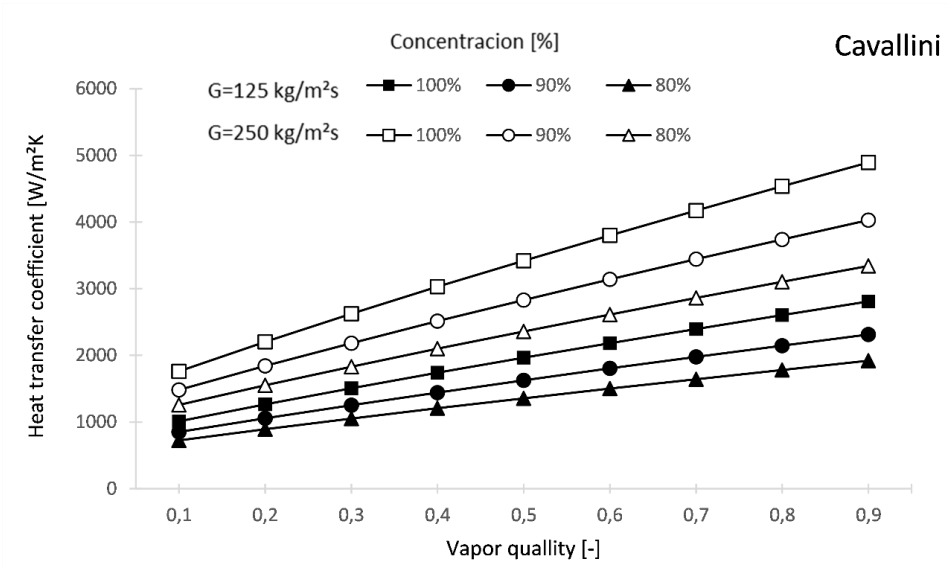

Figure 10: Heat transfer coefficient based on the Cavallini correlation [10]

4. Conclusion

The thermodynamic properties, density, and kinematic viscosity, of the R152a, R125, R134a and R123 refrigerants and POE 68 ester oil mixture, were investigated as a function of refrigerant temperature.

It was found that the density values of the R134a/POE 68 and R123/POE 68 mixtures showed the same trend, with lower density values at 80% concentration than those of the pure refrigerant.

It must be also emphasized that for R152a/POE 68 and R125/POE 68 the density values were almost identical for 80%, 90% and 100% concentration.

For the mixtures R152a/POE 68, R125/POE 68, R134a/POE 68 and R123/POE 68, the change in kinematic viscosity values was the same as a function of temperature. Experiments highlighted that the mixture R123/POE68 had the highest density and kinematic viscosity of all investigated mixtures: 1.6 g/cc respectively 1.5 CSt. Furthermore, it was determined that with the increase of concentration, all four mixtures presented a strong increasing trend of the kinematic viscosity.

Besides this, it must be highlighted that the density values of all mixtures were significantly lower than the density of the pure refrigerant.

In conclusion, increasing the proportion of ester oil in the mixture concentration had a negative effect on the amount of heat transferred during

convective heat flow and also on the heat transfer coefficient Eq. (2). *Fig. 9* and *Fig. 10* showed the effect of the mixture of refrigerant and oil on the values of the heat transfer coefficient as a function of vapor quality and heat mass flux. Two condensation heat transfer models were investigated, namely the Shah and Cavallini correlations. In both cases, it can be seen that as the proportion of oil increases, the values of the heat transfer coefficient decrease.

References

[1] Santa, R., "Comparative Analysis of Heat Pump System with IHX Using R1234yf and R134a", *Periodica Polytechnica Mech. Eng.*, vol. 65, pp. 1–11, 2021.

[2] Kassai, M., "Investigation of the thermal behavior and energy consumption of refrigeration systems", *Thermal Science*, vol. 25, no. 1 Part A, pp. 73–83, 2021.

[3] Sánta, R., Garbai, L., Fürstner, I., "Optimization of heat pump system", *Energy*, vol. 89 pp. 45–54, 2015.

[4] Sánta, R., Garbai, L., Fürstner, I., "Numerical investigation of the heat pump system", *J. Thermal Cal*., vol. 130, no. 2, pp. 1133–1144, 2017.

[5] Santa, R., "The Analysis of Two-phase Condensation Heat Transfer Models Based on the Comparison of Boundary Condition", *Acta Poly. Hun*., vol.9, no. 6, pp. 167–180, 2012.

[6] Santa, R., Garbai, L., "Measurement testing of heat transfer coefficients in the evaporator and condenser of heat pumps", *J. Thermal Cal.*, vol. 119, no. 3, pp. 2099–2106, 2015.

[7] Garbai, L., "Csőhálózatok hidraulikája: Állandósult áramlás", Akadémiai Kiadó, Budapest, 2018

[8] Thomas, J., Bruno, T.J., Fortin, M. L., Huber, A.L., Eric W. L., Elisabeth M., Mark O. M., Stephanie L. O., Richard A. P., Kimberly, N. U., Jason A. W., "Thermophysical Properties of Polyol Ester Lubricants", *NIST Director and Undersecretary of Commerce for Standards and Technology*, 2019.

[9] Shah, M. M., "A General Correlation for Heat Transfer during Film Condensation inside Pipes", *International Journal of Heat and Mass Transfer* 22, no.4, pp: 547–56, 1979.

[10] Cavallini, A., and R. Zecchin, "A dimensionless correlation for heat transfer in forced convection condensation", in *Proceedings of the Fifth International Heat Transfer Conference, Tokyo*, 1974, pp. 309–313.

Acta Universitatis Sapientiae
Electrical and Mechanical Engineering, 13 (2021) 25–38

DOI: 10.2478/auseme-2021-0003

Kinematic and Dynamic Modeling of the Rotary Harrow

Ferenc TOLVALY-ROSCA[1], Judit PÁSZTOR[2], Zoltán FORGÓ[3]

Sapientia Hungarian University of Transylvania, Cluj-Napoca,
Faculty of Technical and Human Sciences, Târgu Mureş,
Department of Mechanical Engineering,
e-mail: [1]tferi@ms.sapientia.ro, [2]pjudit@ms.sapientia.ro, [3]zforgo@ms.sapientia.ro

Manuscript received November 15, 2021; revised December 02, 2021.

Abstract: The actual energy situation and the significant energy demand of agricultural production require the exploration and analysis of the general laws of the main processes in the field of energy, which is part of the borderline between the technical sciences and the agricultural sciences. Tillage machines change the physical properties of the soil, but at the same time the mechanical properties of the soil react to the implement. One of the basic works of seedbed preparation is harrowing. In this work we study the kinematics and dynamics of the active rotary harrow implements, taking into account the cutting resistance of the soil. The results obtained with the developed modeling methods, give reliable approximations to the experienced tilling processes.

Keywords: Rotary harrow, kinematics, dynamics, assembly model.

1. Introduction

Tillage is a mechanical intervention, the aim of which is to create favorable soil conditions for the crops to grow. Tillage consists of basic operations and seedbed preparation. The basic operation is the deepest, the seedbed preparation is shallower, but the most demanding intervention.

The purpose of seedbed preparation is rapid germination, which is facilitated by a soil condition in which the circulation of moisture, air and heat is favorable. During seedbed preparation, the top layer of soil is loosened, crushed, levelled and compacted at the depth of sowing. It is necessary to choose a method and a tool by which the conditions of good germination can be realized cost-effectively with little intervention, without damaging the soil structure. Machines that perform these jobs in one run at the same time are common. These machines are usually equipped with active tillage implements, which are driven by the tractor's PTO shaft. One such work machine is the rotary harrow [1], [2].

The rotary harrow is the seedbed preparation work machine. In the course of its work, it shreds the soil. It also stirs up, flattens and mixes vigorously while shreds. The rotary harrow is power-driven, its implements are active, and they are also driven from the power take-off shaft (PTO), during towing. Thus, the power requirement of the traction work is lower, the slip loss during towing is smaller, therefore it can be used even in wetter ground conditions [1], [3].

The main goal of the machine operation is to provide the required seedbed with the lowest possible number of turns and favorable energy consumption [4], [5].

Using a nonlinear mathematical modeling and simulation of the systems [6] [7], the movement trajectories of a work tool can be studied, [1], [3], [8], [9], [10], [11].

Dynamic models can be used to study the dynamic behaviour [12] and the energy demand [13] of a work tool. In the present paper we perform kinematic and dynamic modelling of the rotary harrow teeth.

2. Materials and methods

We perform kinematic and dynamic modeling of the rotary harrow. To do this, we made a simplified assembly model of the rotary harrow, which is used for dynamic modeling. The trajectories of the harrow teeth are generated using mathematical modeling, the forces acting on one harrow tooth are determined, then they are used to make computer simulations for dynamic and energetic studies.

2.1. The simplified assembly model

The working tool of the rotary harrow is the tine. Since the rotation direction of the adjacent work units is opposite, two types of tines are used according to each rotation directions (*Fig. 1*).

Figure 1: The solid models of the tines (left) and a working unit with two tines (right)

The implements are driven from the power take-off shaft of the power unit, via a deceleration gearbox (*Fig. 2*). The PTO shaft spindle speed is conventional, 540 rpm. The drive chain is designed so that the rotational movement from the tractor-PTO is transmitted by gears to the vertical axes, so that the adjacent implements rotate in opposite directions.

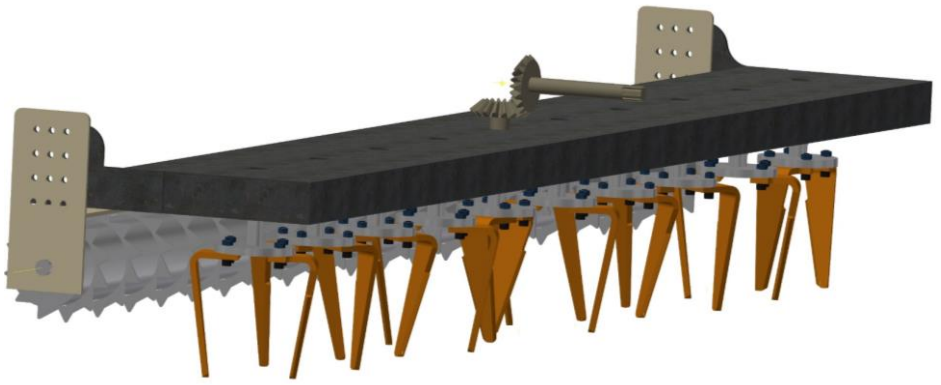

Figure 2: The simplified assembly model of the rotary harrow is based on Amazone KE3001 type machine [14]

The shapes of the harrow tines are extremely various. Most work machine manufacturers reduce fuel consumption and wear by using new, optimized shapes and innovative materials to increase the efficiency of their products [8].

The most commonly used harrow tine is the wide-bladed harrow tine. It can be made in straight or helical, vertical or oblique versions. In this paper we analyze a wide-bladed, oblique harrow tine. The width of the harrow tines increases from the tip to the base, so the cutting edge is able to pull the plant stalks into the soil, hence it has a slight compacting effect in the working depth and avoids any obstacles more easily.

2.2. The kinematic model

The trajectories of the points situated on the tines are important parts of the kinematic models. The trajectories can be used to identify parameters that affect tooth movement and to analyze how they affect the tillage process. The dimensions of soil chips formed during the movement of harrow tines in the soil can also be analyzed [10].

The points noted with $A_i(x_{Ai}, y_{Ai}, z_{Ai})$ and $B_i(x_{Bi}, y_{Bi}, z_{Bi})$, $i = 1 \div 10$ represent the tip of the harrow tines. The tines are moved by the combined effect of a rotating and a forward (towing) movement (*Fig. 3*).

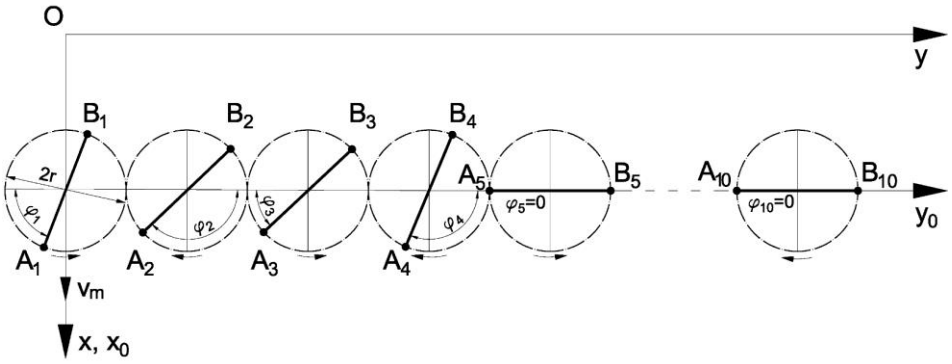

Figure 3: The initial positions of the working units, according to Amazone KE 3001 [14]

The motion equations of the points $A_i(x_{Ai}, y_{Ai}, z_{Ai})$ and $B_i(x_{Bi}, y_{Bi}, z_{Bi})$ in the stationary coordinate system $°xO°y$ are given by the following relations:

$$ {}^{o}A_i \begin{cases} {}^{o}x_{Ai} = r_t \sin\left((-1)^i\theta + \varphi_i\right) + v_m t \\ {}^{o}y_{Ai} = 2r(i-1) + r_t \cos\left((-1)^i\theta + \varphi_i\right) \\ {}^{o}z_{Ai} = -a \end{cases} \tag{1} $$

$$ {}^{o}B_i \begin{cases} {}^{o}x_{Bi} = r_t \sin\left((-1)^i\theta + \varphi_i + \pi\right) + v_m t \\ {}^{o}y_{Bi} = 2r(i-1) + r_t \cos\left((-1)^{\mathrm{i}}\theta + \varphi_i + \pi\right) \\ {}^{o}z_{Bi} = -a \end{cases} \tag{2} $$

$$ \theta = \varpi t \tag{3} $$

where: v_m is the forward speed of the rotary harrow, [m/s]; ω is the angular velocity of the drive shaft, [rad/s]; a is the working depth [m]; i is the serial number of the implement; φ_i is the angle between the direction line of the working units and the horizontal line - the initial phase shift, r is the radius of the rolling circle of the gears, r_t is the half distance between the tips of the tines from a working unit.

Note: for i = 5 the above relations describe the driving unit; r_t depends on the shape of the tine: if $2r_t = 2r$, the tines are vertical, if $2r_t > 2r$ the tines are divergent and if $2r_t < 2r$ the tines are convergent (the tines are tilted).

The initial phase shifts of each working unit φ_i are given in *Table 1*:

Table 1: Initial phase shifts for each work unit

φ_1	φ_2	φ_3	φ_4	φ_5	φ_6	φ_7	φ_8	φ_9	φ_{10}
π/3	5π/6	π/6	2π/3	0	2π/3	π/6	5π/6	π/3	0

According to the motion equations, the trajectories of the tines describe looped cycloids (*Fig. 4*) [15]. The equations are considered valid and suitable to perform kinematic studies.

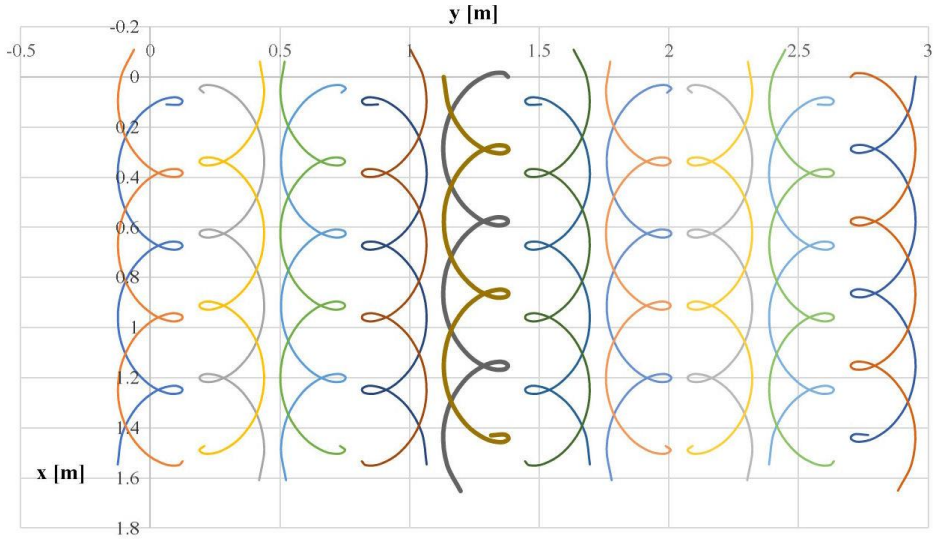

Figure 4: The rotating harrow tine tips trajectories

We examined the effect of changes of the tilt angle of the harrow tines, the towing speed, and the angular velocity on moving trajectories.

The effect of the tilt angle of the harrow tines in the cultivated soil, as a function of the working depth, can be seen in *Fig. 5*.

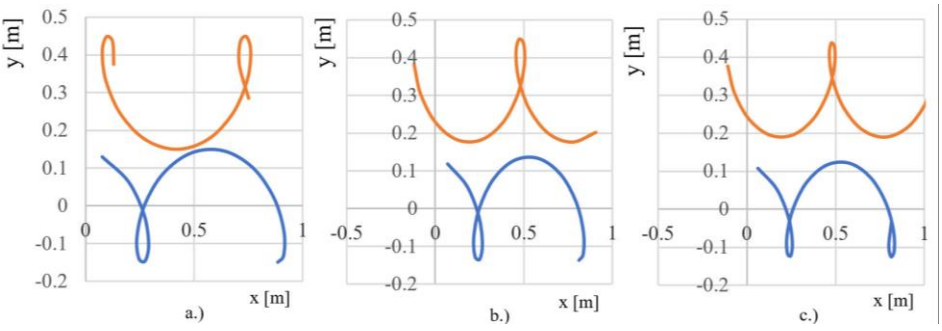

Figure 5: Trajectories described by points in different depths of the tine.
a.) top of harrow tine, b.) middle of harrow tine, c.) tip of the harrow tine

Due to the cohesiveness of the teeth, the distance between the sides of the teeth decreases from the surface of the soil to the tip of the teeth. Thus, soil shredding is expected to be more vigorous close to the surface relative to the working depth. Thus, the inclination angle contributes to the proper formation of the seedbed.

The effect of the forward speed on the worked surface can be seen in *Fig. 6*. As the forward speed increases, the stride of the implement increases, and the cuts become less frequent. As a result, the seedbed becomes clumpier and may require further processing.

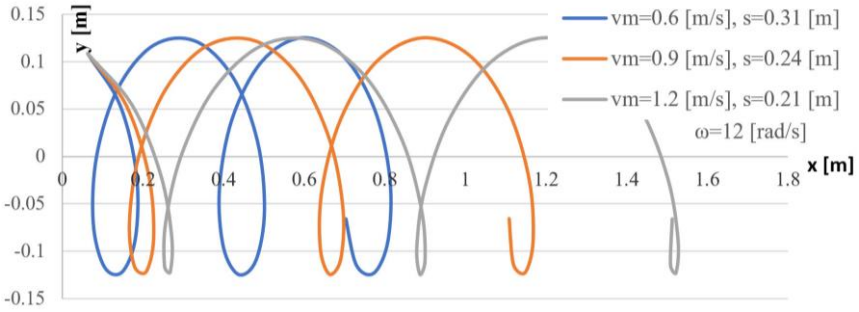

Figure 6: The effect of the towing speed on the trajectory of the tip

In practice as an illustrative indicator, the step of the implement [9], is used to characterize the kinematics of the work process. In the case of a rotary harrow, step *s*, the distance made during one revolution, can be calculated as follows:

$$s = v_m T = v_m \frac{2\pi}{\omega}; \qquad s = \frac{v_m}{n}\,[\mathrm{m/rot}] \tag{4}$$

where: T [s], period of rotating motion and n [rpm] the spindle speed.

It can be concluded, that the pitch of the rotary harrow varies in direct proportion to the forward speed and in inverse proportion to the speed.

The effect of the angular velocity on the worked surface can be seen in *Fig. 7*. A low angular velocity results in a less machined surface.

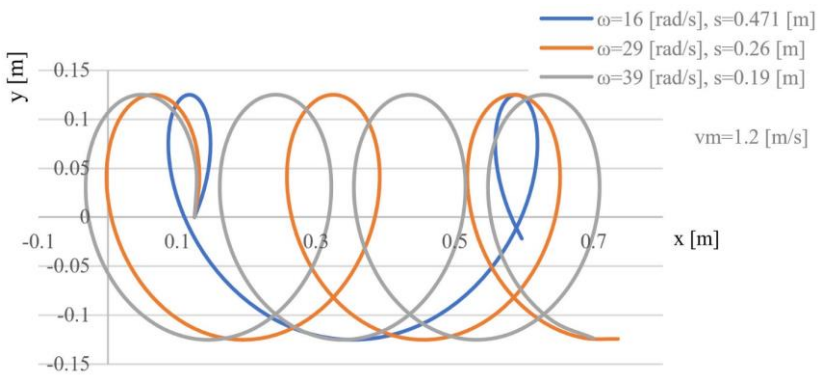

Figure 7: The variation of the tip trajectory for different angular velocities of the working unit

The rotary harrow's kinematic index is given by:

$$\lambda = \frac{v_p}{v_m} = \frac{\omega\, r}{v_m}\ [-] \tag{5}$$

Recommended values based on operating experience: $\lambda = 1.5 \div 6$, [11], [14]. In the investigated cases: $\lambda = 1.25 \div 2.50$, $\lambda = 1.66 \div 4.06$.

2.3. Dynamic modeling

In this paper, we consider the work of the tines divided into two elementary processes. The tines cut and compress the soil.

According to these processes in *Fig. 8*, the following forces are considered:

- the bit force (F_b);
- the friction forces (T_1 and T_2) - on the sides of the tine;
- the normal forces (N_1 and N_2) - acting on the tine sides;
- the compaction forces, F_c.

The forces acting on the tine were calculated based on literature data [16], [17], [18].

Determining the forces and the loads on the implements, which result from a real tillage of the soil, is a complex task, as the stresses already laying in the soil can also influence the soil's response to tillage forces, and these should be incorporated into the models, [19].

2.3.1. Determination of the Bit Force

The tine is considered a wedge-type blade having a pentagonal cross-section with parallel sides (*Fig. 8*) [16], [20], [21].

The tine, due to the work of the previous tine, also travels in shredded-loosened-pre-compacted soil, so the deformation zone will be asymmetrical. As a result of the change in the deformation zone, the forces acting on the tool also change. In determining the shear force, it is assumed that the physical properties of the soil are different on both sides of the harrow tooth, so the soil can be considered more compact on one side.

The forces acting on the wedge, in the light of the above, are shown in *Fig. 8*. The resulting force on the wedge is given by the sum of the normal forces N and the frictional forces T, acting on the wedge. The occasionally concentrated loads (given by stones, roots etc.) acting on the tool edge are not taken into consideration in our model.

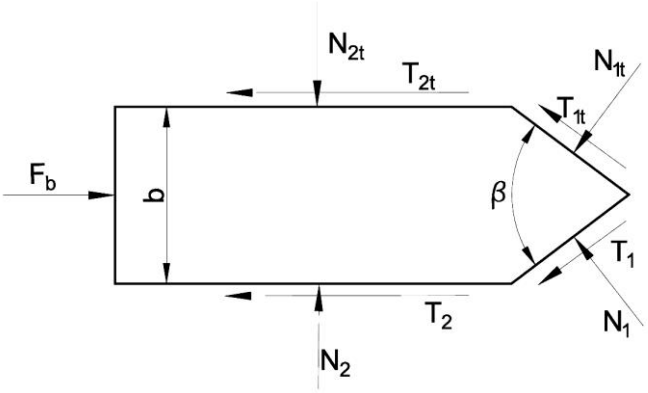

Figure 8: The forces acting in a section of a tine

The bit force acting on the tine can be calculated using the cutting resistance. It derives from normal forces and frictional forces, where:

$$N_{1t} = k_{1t}A_1 \text{ [N]}, N_1 = k_1A_1 \text{ [N]} \tag{6}$$

$$T_{1\mathrm{t}} = \mu_t N_{1\mathrm{t}} = \mu_t k_{1\mathrm{t}} A_1 \text{ [N]},\ T_1 = \mu N_1 = \mu k_1 A_1 \text{ [N]} \tag{7}$$

$$N_{2\mathrm{t}} = k_{2\mathrm{t}}A_2 \text{ [N]}, N_2 = k_2A_2 \text{ [N]} \tag{8}$$

$$T_{2\mathrm{t}} = \mu_t N_{2\mathrm{t}} = \mu_t k_{2\mathrm{t}} A_2 \text{ [N]},\quad T_2 = \mu N_{2\mathrm{k}} = \mu k_2 A_2 \text{ [N]} \tag{9}$$

$$F_b = N_1 \sin\frac{\beta}{2} + T_1 \cos\frac{\beta}{2} + T_2 + N_{1t} \sin\frac{\beta}{2} + T_{1t} \cos\frac{\beta}{2} + T_{2t} \text{ [N]} \tag{10}$$

where: k_{1t}, k_{2t}, are the specific resistances to worked soil deformation [N/m^2]; k_1, k_2 are the specific resistances to unworked soil deformation [N/m^2]; A_1 is the active surface of the tine edges [m^2]; A_2 is the surface of one of the sides of the

tine in contact with the soil [m^2]; μ_t, μ are the friction coefficients between the soil and the tine; and β is the lip angle of the tine.

During the work the A_1 and A_2 surface can be considered functions of the working depth a [m], $A_1 = f_1(a),\ A_2 = f_2(a)$.

The k_1 and k_2 coefficients depend on: the soil deformation – are functions of thickness of the tine, the friction coefficient between the soil and the tine and the soil texture type. According to [12] $k_1, k_2 = f(b, \beta, \varphi)$, where b is the harrow tine thickness [m].

The values of the above coefficients are $\mu_t = 0.6$ and $\mu = 0.7$; $k_{1t} = 720883.68$ [N/m^2], $k_1 = 783930.62$ [N/m^2], $k_{2t} = 33692.35$ [N/m^2], $k_2 = 32128$ [N/m^2]; $\beta = 90°$ and $b = 0.015$ m.

2.3.2. Calculating the compaction forces, Fc

The harrow tines shred the soil, while they rotate during the work, compacting the soil in the towing direction. This process, shown in *Fig. 9*, can be considered a cutting with a variable wide profile (the projection of the width changes according to the rotation angle) [16]. The maximal width of the profile in this case is the length of the side of the tine.

To determine the compaction forces, the physical and mechanical properties of the soil, the geometry of the cutting tool must be considered [22].

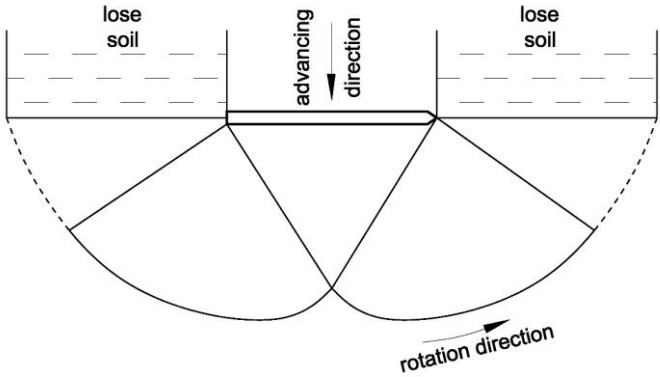

Figure 9: The compaction effect of the tine

To calculate soil resistance, the international literature uses the equation of Reece [18]. Cutting resistance per unit width:

$$f_c = \gamma a^2 N_\gamma + caN_c + a_{adh}aN_a + qaN_q \left[\frac{\mathrm{N}}{\mathrm{m}}\right] \tag{11}$$

where: a is the working depth [m]; γ is the specific weight of soil [N/m^3]; c is the soil cohesion [N/m^2]; a_{adh} is the soil adhesion [N/m^2]; q surcharge on the soil surface [N/m^2]; N_c, N_γ, N_a, N_q are dimensionless Reece's resistance factors.

Reece's resistance factors are function of friction factors (ρ and φ), tool geometry, and deformation zone formation. Values used in the calculation: γ = 1500·9.81=14715 [N/m^3]; c = (0.01…0.02) ·10^4 [N/m^2]; a_{adh} = 0 [N/m^2]; q = 0 [N/m^2]; Reece's resistance factors: N_c = 4.8, N_γ=8.8 (ρ = φ = 35°, α = 90° [16]).

The compaction force acting on a tine changes during its circular motion (*Fig.10*), and depends on the projected width of the harrow tine:

$$F_c = f_c\, l \cos\theta = f_c\, l \cos\omega t \text{ [N]} \tag{12}$$

where: l is the median width of the tine (at the half of the working depth a) [m].

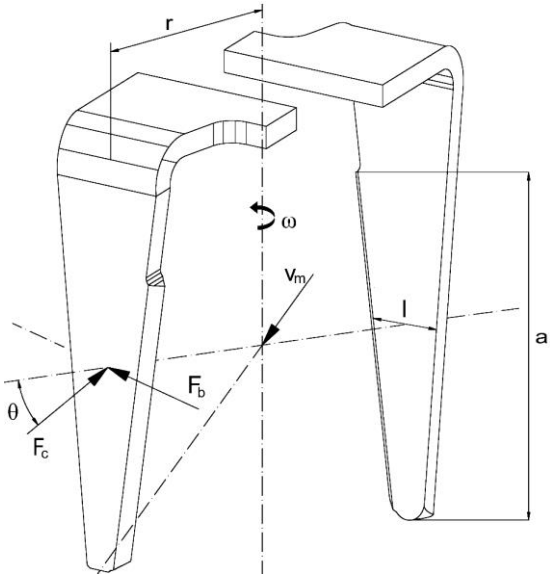

Figure 10: The position of the bit (F_b) and compacting (F_c) loads regarding the tines

2.4. Determining the driving torque

The paper [23] presents a methodology for mechanism simulation in case of agricultural machines, which may be applied at this mechanism also as seen in *Fig. 11.*

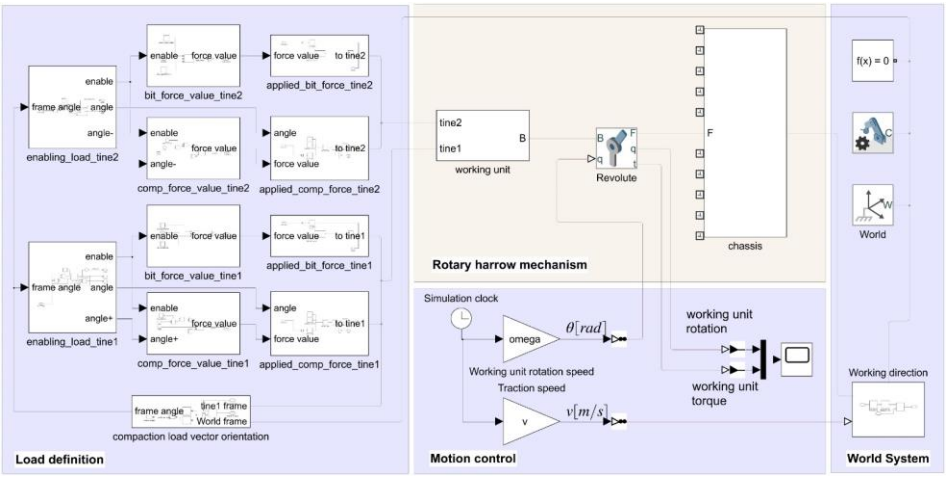

Figure 11: The Matlab Simscape model of the rotary harrow mechanism containing the working loads and kinematic parameters of the working process

The core element of the model is the rotary harrow mechanism area, which was presented already in *Fig. 2*. Because of model redundancy, the mechanism is simplified: besides the chassis, only one working unit is considered. This will allow a quicker simulation, and further, to obtain the driving torque for the whole rotary harrow machine, the number of the working units must multiply the simulation result. Overlapping the 10 torque variations through time must be done by taking into consideration the initial phase shifts depicted in *Table 1*.

Next to the *Rotary harrow mechanism* area, the *Motion control* allows to run the simulation with the kinematic parameters as *v* for the traction speed and *omega* for the working unit rotation speed. To obtain the needed driving torque for the working unit, the loads on the tines must be calculated and applied at the right timing intervals. As above presented (*Fig. 10.*), two loads were taken into account, whose definitions are provided in equations (10) and (12). The *Load definition* area from the simulation implements those equations and applies to the tines of the working unit (denoted by *tine1* and *tine2*). The magnitude and the direction of the loads are the same for both of tines, but the applying time interval differs through the simulation. Therefore, to have a more readable simulation model, the loads are calculated and presented separately.

The calculated driving torque for one working unit could be retrieved from the simulation through the graph element inside the *Motion control* area. Applying the phase shifts between the working units and summing the overall torques, for the parameters v = 1m/s traction speed and *omega* = 16 rad/s working unit rotation speed, the final simulation result is obtained.

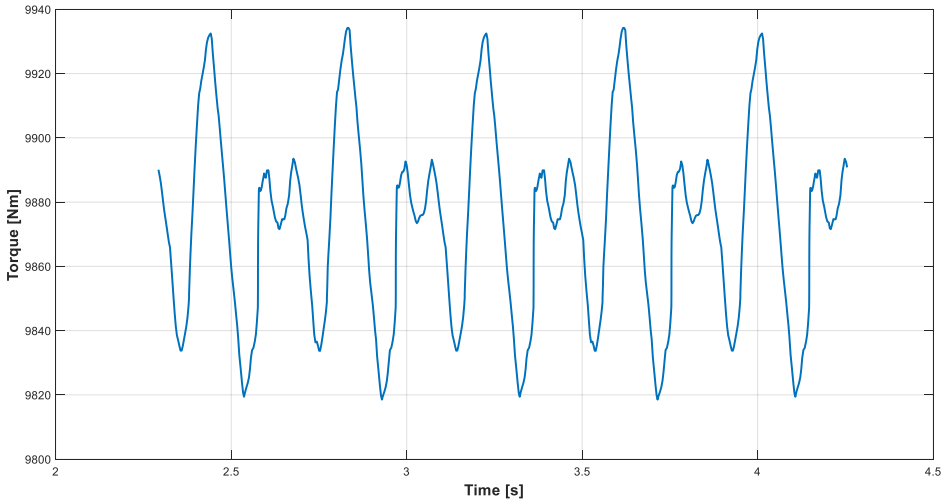

Figure 12: The variation of the driving torque (five cycles depicted)

Fig. 12. presents the torque variation through [2.25 s, 4.25 s] time interval consisting of five cycles. The mean value for the driving torque is 9872.6 Nm, having a cyclic variation in the [9818.5 Nm, 9934.2 Nm] interval.

3. Conclusions

The above defined kinematic equations describe trajectories also found in the literature, so they are suitable for performing theoretical investigations. As they are graphically visualized in a virtual environment, they easily allow to track changes made to various working parameters.

As the towing speed and the implement's spindle speed majorly affects the quality and the bumpiness of soil work to be performed, it is recommended to carefully choose the values for these parameters.

We can also state that the further development of soil preparation machines is inconceivable without a solid knowledge of the soils and their characteristics. The complex structure and inhomogeneity of soils make it very difficult to describe their general mechanical laws and to select the correct mechanical properties. The main difficulty in modeling a close to reality soil-machine relationship is to build a complex computer model of the soil. While tillage machines change the physical properties of the soil, they also have reactions on the implement. The currently used soil characteristics do not describe correctly the mechanical behavior of soils under all conditions. In the presented modeling process, we performed simplifications that take from the complexity of the tillage processes. The presented work can be used as base for further practical and experimental investigations.

References

[1] Láng, Z., "A zöldség-, dísznövény- és szaporítóanyag – termesztés berendezései és gépei", Publisher Mezőgazda, Budapest, 1999.

[2] Szendrő, P., "Géptan", Publisher Mezőgazda, Budapest, 2003.

[3] Pásztor, J., Forgó, Z., "Ásógép kinematikája és munkaminőségi mutatóinak vizsgálata növényházban", *Műszaki Szemle, Publisher EMT, Cluj-Napoca*, 2009.

[4] Birkás, M., Dekemati, I., Kende, Z., Radics, Z., Szemők, A., "A sokszántásos műveléstől a direktvetésig-Előrehaladás a talaj művelésében és védelmében", *Agrokémia és Talajtan*, no.67, vol. 2, pp.253–268, 2018.

[5] Raparelli, T., Pepe, G., Ivanov, A., Eula, G., "Kinematic Analysis of Rotary Harrows", *Journal of Agricultural Engineering*; vol. LI:976, pp. 9–14, 2020.

[6] Kovari, A., "Effect of Leakage in Electrohydraulic Servo Systems Based on Complex Nonlinear Mathematical Model and Experimental Results", *Acta Polytechnica Hungarica*, vol. 12, no. 3, pp. 129–146, 2015.

[7] Sánta, R., Garbai L., Fürstner, I., "Numerical Investigation of the Heat Pump System", *Journal of thermal analysis and calorimetry*, vol. 130, no 2, pp. 1133–1144, 2017.

[8] Balsari, P., et al., "Performance Analysis of a Tractor - Power Harrow System Under Different Working Conditions", *Biosystems Engineering*, vol. 202, pp. 28–41, 2021.

[9] Major, T., "Mechanization Development for Soil Tillage at Stumpy Forest Areas", *Theses of doctoral (PhD) dissertation, University of West Hungary, Sopron*, 2014, http://doktori.nyme.hu/458/2/ Tezisfuzet_angol_MajorT.pdf.

[10] Virág, S., "Effects of Cultivation on Clod Formation os Soils Energetic Relationships in Breakage of Clods", *Theses of doctoral (PhD) dissertation, University of Debrecen*, 2005, https://dea.lib.unideb.hu/dea/handle/2437/79555.

[11] Naghiu, A., Baraldi, G., Naghiu, L., "Mașini și instalații agricole", *Editura Risopront, Cluj-Napoca*, 2004.

[12] Kovari, A., "Influence of Cylinder Leakage on Dynamic Behavior of Electrohydraulic Servo System," in *SISY 2009 - 7th International Symposium on Intelligent Systems and Informatics*, 2009, pp. 375–379.

[13] Sánta, R., "Comparative Analysis of Heat Pump System with IHX using R1234yf and R134a", *Periodica Polytechnica Mechanical Engineering*.

[14] https://amazone.hu/hu-hu.

[15] Máté, M., "Műszaki mechanika – kinematika", *Publisher TMS, Cluj-Napoca*, 2010.

[16] Sitkei, Gy. "Soil Mechanics Problems of Agricultural Machines", *Publisher Franklin Book Programs, New York, U.S.A.*, 1976, pp. 22–62.

[17] Major, T., Csanády, V., "Application of Numerical Analysis for the Design of Rotating Tool", *Hungarian Agricultural Engineering*, no. 26/2014, pp. 16–19, 2014.

[18] Chung, S. O., Sudduth, K. A, "Soil Failure Models for Vertically Operating and Horizontally Operating Strength Sensors", *American Society of Agricultural and Biological Engineers*, vol. 49(4), pp.851–863, 2006.

[19] Rajaram, G. "Mechanical Behavior of an Agricultural Soil", *Retrospective Theses and Dissertations. 9570, Iowa State University, Capstones*, 1991.

[20] Amantayev, M., Gaifullin. G., Nukeshev, S., "Modelling of the Soil-Two Dimensional Shearing Tine Interaction", *Bulgarian Journal of Agricultural Science*, 23, no.5, pp. 882–885, 2017.

[21] Aluko, O.; Seig, D. A., "An Experimental Investigation of the Characteristics of and Conditions for Brittle Fracture in Two-Dimensional Soil Cutting", *Soil & Tillage Research*, vol. 57, no.3, pp.143–157, November 2000.